3-D Radiometric Aperture Synthesis Imaging

Neil A. Salmon

***Abstract*—The aperture synthesis technique, historically used for imaging in radio astronomy, is generalized to three dimensions as a means to generating 3-D images in the near-field. The technique uses a multi-channel electronic cross-correlator and an array of radio receivers to generate a 3-D visibility function. This is transformed by a 3-D inverse Fourier transform into a 3-D image of space. The basic equations, experimentation, and simulation indicate the Abbe microscope half-wavelength spatial resolution is achievable in three dimensions when a subject is surrounded by receivers. At longer ranges, further from the array, the resolution perpendicular to the range is proportional to the ratio of the range to aperture size (corresponding to the Fraunhofer diffraction limit) while the resolution in range is proportional to the square of this ratio (a passive ranging capability). Experimental data from a 10-channel 94-GHz and a 32-channel 22-GHz receiver array and a digital cross-correlator demonstrate the imaging capability. The technique enables arbitrarily large volumes to be imaged using multiple inverse 3-D Fourier transforms for adjacent regions of space, when suitable phase corrections are applied to cross-correlations. The technique is mainly directed at the millimeter-wave band for the application of personnel security screening.**

***Index Terms*—Aperture synthesis, imaging, millimeter wave, near-field, security screening, 3-D.**

I. Introduction

In THE 1930s, van Cittert and Zernike concluded [1] that the cross-correlation $V_{J,K}$ of electric fields $v_J(t)$ and $v_K(t)$ at two locations from an extended source $I(S)$ is given by the surface integral over the surface of the source σ, as in (1), where r_J and r_K are the distances from the source to the two locations, k is the wavenumber of the radiation, and $*$ is the complex conjugate. This result is referred to as the generalized van Cittert Zernike (VCZ) theorem. In the far-field it becomes a Fourier transform relationship between the source function and the cross-correlations. Placing many pairs of cross-correlations on a 2-D far-field spatial frequency abscissa (defined as distance between pairs of antennas divided by the radiation wavelength λ) creates the visibility function. The 2-D inverse Fourier transform of the visibility function creates an image of the source and this is the basis of the radio astronomy aperture synthesis technique [2],

$$V'_{J,K} = \langle v_J(t) v_K^*(t) \rangle = \int_\sigma [I(S)/r_J r_K] \exp[ik(r_J - r_K)]\, dS. \quad (1)$$

In 1981, Carter and Wolf showed [3] that the generalized VCZ theorem has a 3-D Fourier transform relationship to the source in the far-field. Furthermore, in 1989, Carter adapted [4] the standard 2-D far-field technique of aperture synthesis so it could be used in the near-field Fresnel regime, namely, at ranges closer than the Rayleigh range, $2D^2/\lambda$, where D is the longest baseline of the receiver array. In 1993, Zarubin recognized [5] the 3-D VCT could be inverted to obtain 3-D spatial information at the atomic level from the scattering of X-rays, electrons, and neutron waves. In 1996, Rosen and Yariv proposed [6] the use of a Michelson interferometer to measure the correlation as a means to generating 3-D images of objects via the VCZ theorem. In 1999, Marks *et al.* used [7] an optical rotational shear interferometer to make 3-D images in the near-field using this principle. In 2007, a fiber optic Michelson interferometer measured correlations from scattered near-infrared laser radiation to generate 3-D volumetric images of biological cells, naming the technique interferometric synthetic aperture microscopy (ISAM) [8].

The work presented in this paper, as above, exploits the VCZ theorem to generate 3-D images, but differs in two key respects. Firstly, the sources of radiation are radiometric, meaning emission is spatially and temporally incoherent and the intensity is proportional to object temperature. Secondly, as the frequency is low, radio technology can be used to sample directly electric fields spatially using antenna arrays, avoiding the use of lenses and their problems of aberrations. This means antenna arrays can sample up to the full 4π steradians of space surrounding an object, enabling snap-shot 3-D imaging, without the need for mechanical scanning, constituting a form of diffraction emission tomography [9].

Section II describes the 3-D imaging algorithm, which exploits the generalized VCZ theorem and the concept of near-field local 3-D spatial frequencies. Section III discusses the antenna array topologies, which are used to spatially sample the radiometric electric fields, respecting the Nyquist criterion and how to minimize the effects of aliasing. Section IV derives from first principles the expressions for the spatial resolutions of the 3-D imaging technique, relating them to the classical Abbe microscope resolution $(\lambda/2)$ and the Fraunhofer diffraction limit (λ/D). Section V discusses the 3-D field-of-view of the imaging technique in the near-field, when the Fresnel approximation breaks down, and the importance of the Fresnel

Manuscript received December 17, 2014; revised April 03, 2015 and August 01, 2015; accepted September 14, 2015. Date of publication October 07, 2015; date of current version November 03, 2015. This work was supported in part by a Royal Society Industry Fellowship, the Department of Trade and Industry (now Innovate UK) "Basic Technologies for Industrial Applications Programme," the European Space Agency "Terahertz Camera" initiative, the University of Manchester, and QinetiQ Ltd.

The author is with the Faculty of Science and Engineering, Manchester Metropolitan University, Manchester M15 6BH, U.K. (e-mail: n.salmon@mmu.ac.uk).

Color versions of one or more of the figures in this paper are available online at http://ieeexplore.ieee.org.

Digital Object Identifier 10.1109/TMTT.2015.2481413

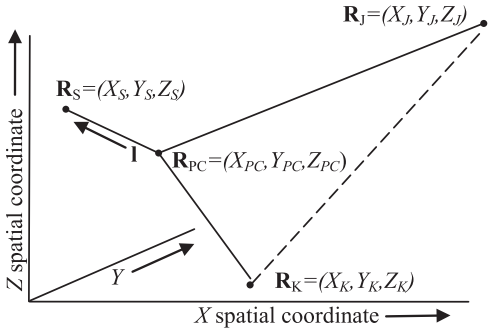

Fig. 1. Coordinate system of the 3-D aperture synthesis imaging technique, showing the position vectors of: an element of the source $\mathbf{R}_S$, the phase center $\mathbf{R}_{\mathrm{PC}}$ (the center of the 3-D source and the resulting image), a pair of measurements antennas, $\mathbf{R}_J$ and $\mathbf{R}_K$, and the distance vector $\mathbf{l}$ from the phase center to an element of the source. The dotted line is the J, K antenna base-line.

scale parameter. Section VI describes the instrument used to realize the 3-D aperture synthesis imaging technique and presents the experimental evidence to support this claim. Section VII presents a forward simulation technique to create synthetic cross-correlations from scenes, which are then converted into 3-D images using the algorithm of Section II, and subsequently used to demonstrate the limiting resolutions and fields-of-view predicted in Section IV and V.

II. 3-D Imaging Algorithm

From the Carter and Wolf generalization of the VCZ theorem [3], the 3-D visibility function $V(\mathbf{u})$ is related to the 3-D far-field image $I(\mathbf{l})$ by (2), where $\mathbf{u}$ is the local spatial frequency in vector notation (for the three x, y,and z spatial coordinates) and $\mathbf{l}$ is the displacement (i.e., distance) vector from a phase center at a position vector $\mathbf{R}_{\mathrm{PC}}$ (nominally at the center of the source) to an element of the source at a location $\mathbf{R}_S$, as illustrated in Fig. 1. The antenna pattern of the individual receivers is given as $A(\mathbf{l})$, referred to hereafter as the primary beam-pattern, to distinguish it from the synthesized (narrower) beam-pattern of the complete array of antennas. The limits of the integration, $\mathbf{u}_{\mathrm{MIN}}$ and $\mathbf{u}_{\mathrm{MAX}}$, are defined by the receiving antennas that have the maximum angular displacements from each other. As the image $I(\mathbf{l})$ contains intensity information only, the visibility function $V(\mathbf{u})$ is Hermitian. This means that each cross-correlation contributes a Hermitian conjugates pair of data points to the 3-D visibility function,

$$I(\mathbf{l}) = [A(\mathbf{l})]^{-1} \int_{\mathbf{u}_{\mathrm{MIN}}}^{\mathbf{u}_{\mathrm{MAX}}} V(\mathbf{u}) exp(i2\pi \mathbf{u}.\mathbf{l}) d^3u. \tag{2}$$

In classical aperture synthesis imaging, used for a number of decades in radio astronomy, and more recently for earth observation from satellites [10], [11], (2) is simplified from three to two dimensions and a 2-D image of the source in the far-field is created by a 2-D Fourier transform of a 2-D visibility function. The pioneering work in [10] and [11] also led to the accepted form of the radiometer equation for sparse arrays. This states that the noise on the radiation temperatures in the resultant image ΔT is given by (3), where T_A and T_R are the mean scene radiation and receiver noise temperatures, respectively, f is the fractional filling of the array, B is the radiation bandwidth of the receivers, and t is the signal integration time. The fractional filling of the array is the ratio of the sum of the individual collecting areas of the antennas in the array to the total area of the array (as if it were completely filled with antennas),

$$\Delta T = \frac{1}{f} \frac{T_A + T_R}{\sqrt{Bt}}. \tag{3}$$

The creation of 3-D images using (2) requires the visibility function $V(\mathbf{u})$ to be sampled, satisfying the Nyquist criterion (and topologies to achieve this are discussed in Section III) before inversion to create the image $I(\mathbf{l})$. The sampled visibilities $V_m(\mathbf{u})$ from the pairs of antennas is described for 2-D antenna arrays in [2], and extending this to three dimensions, it is given by (4), where $s(\mathbf{u})$ is the sampling function (a set of delta functions, each one representing a particular spatial frequency) and F is the 3-D Fourier transform operator. Applying the convolution theorem to this equation indicates each sample of the visibility function is a convolution of the scene visibility function $V(\mathbf{u})$ with the Fourier transform of the primary beam, $A(\mathbf{l})$. The synthesized beam (a much narrower function) is the product of the primary beam and the Fourier transform of the sampling function, $s(\mathbf{u})$. Inversion of the measured visibilities to generate the image $I_m(\mathbf{l})$ is described for two dimensions in [2] with a 3-D generalization given by (5) where F^{-1} is the 3-D inverse Fourier transform operator, and $w(\mathbf{u})$ is a set of user defined weightings. The (5) represents a discretization of (2). Radio astronomers choose various weightings to optimize image quality. These can be used to: 1) compensate for not satisfying the Nyquist sampling criterion at various spatial frequencies; 2) take into consideration primary antenna beam effects; and 3) reduce sidebands on the synthesized beam. In the experimental and simulation work of this paper, all weightings were taken to be unity (referred to by radio astronomers as "natural weighting"), as it consistently delivered the most faithful reproduction of the object in the image,

$$V_m(\mathbf{u}) = s(\mathbf{u}) F\left[I(\mathbf{l}) A(\mathbf{l})\right] \tag{4}$$

$$I_m(\mathbf{l}) = F^{-1}\left[V_m(\mathbf{u}) w(\mathbf{u})\right]. \tag{5}$$

There are two routes to implementing the inverse Fourier transform of (5). The first route is to perform what radio astronomers refer to as a "direct inverse Fourier transform"; this is an exact analytic inverse Fourier transform of the measured visibilities. The alternative route is to interpolate the measure visibilities onto a regular grid, in order that an inverse fast Fourier transform (FFT) algorithm can be used [2]. For the work described here, the latter method was used, as image quality was consistently better with this approach, and is significantly faster, particularly for large numbers of points.

It is important to point out that the work here does differ from that of the radio astronomers in that a 3-D visibility function is processed into a 3-D image. This involves interpolating the 3-D visibilities on to a 3-D cuboidal grid in order that a 3-D inverse FFT can process the data into a 3-D image.

When selecting the regular FFT grid on to which measured or simulated cross-correlations are interpolated, the software identifies if the antennas are already on a regular square or hexag-

onal grid, even if sparsely populated. If a regular grid is identified, this is used as the FFT abscissa, so interpolation errors are minimized. If a random array is detected the smallest absolute spatial frequency in each of the three dimensions from the antenna array is selected. These values, or one-half of a cycle (corresponding to Nyquist sampling), whichever is the greater, are used to set the spacing of the FFT grid. There are options in the software to oversample by integer factors, which increases the number of interpolation points on the FFT grid. However, it was found that in most cases this oversampling made little difference to the final results. As the FFT grid is regular it generally has some baselines in the corner regions, which are longer than those from the antenna array. These regions on the FFT grid are identified and the values of the visibilities at these locations are set to zero. An example of this is shown in Fig. 7(b), whereby a 2-D slice from the 3-D visibility function from a simulation is illustrated. There are options in the software to append zeros onto the visibilities on the FFT grid, which although not adding extra information, does result in smoother surface plots and less pixilated images, which aesthetically is more pleasing.

When interpolating on to the FFT grid there is found to be little difference between the results of nearest neighbor, linear, and cubic spline interpolation. However, cubic spline did on rare occasions generate wild interpolated values so linear interpolation became the default.

As the Fourier transform relationship of (2) between the visibility function and the image is only valid in the far-field, the following considerations must be made when building the visibility function from the cross-correlations before inversion into the 3-D image can proceed. In the near-field, the measured cross-correlations $V'_{J,K}$ need to be phase shifted by an amount $\phi_{J,K}$, as described by (6), to make the phases of cross-correlations generated by sources at the phase center zero. The phase required to do this is given by (7), where $\boldsymbol{R}_J$ and $\boldsymbol{R}_K$ are the position vectors of the J, K receiver antenna pair. This technique of phase shifting the cross-correlations is the first half of the technique proposed by Carter [4] for generating 2-D images of objects in the near-field. The phase shifted cross-correlations can then be placed, together with their complex conjugates, on a 3-D local spatial frequency abscissa. A 3-D interpolation of these cross-correlations $V_{J,K}(\mathbf{u})$ on to the regular cuboidal grid of local spatial frequencies generates the measured values of the visibility function, $V_m(\mathbf{u})$, which can then be inversely Fourier transformed to create the 3-D image. This method of phase shifting the cross-correlations means that the 3-D Fourier transform generates a 3-D image, which is centered on the phase center. The process is rather like a Fresnel transform whereby the function is first phase shifted before applying the Fourier transform. In an experimental scenario, the phases of (7) can be measured directly by recording the cross-correlations generated from a spatially coherent (i.e., point) noise source placed physically at the desired phase center location in the 3-D scene. The technique also conveniently serves to phase calibrate the individual receiver channels and the phases and amplitudes of the cross-correlations in the experiment,

$$V_{J,K}(\mathbf{u}_{J,K}) = V'_{J,K} \exp(-i\phi_{J,K}) \tag{6}$$

$$\phi_{J,K} = (2\pi/\lambda)\left(|\mathbf{R}_J - \mathbf{R}_{PC}| - |\mathbf{R}_K - \mathbf{R}_{PC}|\right). \tag{7}$$

In the near-field, the local spatial frequency is the change in phase of the cross-correlation from a point source as it moves through the 3-D field-of-view, defined [12] mathematically in vector notation in (8). Here, ∇ is the nabla operator, which generates the spatial gradient of the phase of the cross-correlations at the phase center. The local spatial frequency has units of cycles per meter. It is important to make the distinction between this and the far-field spatial frequency, familiar to radio astronomers as being the phase change per angular shift of a point source moving across the sky, nominally the ratio of the distance between the two antennas to the wavelength,

$$\mathbf{u}_{J,K} = \left(\frac{1}{2\pi}\right) \nabla \phi_{J,K}. \tag{8}$$

From the definition of spatial frequency in (8) and the geometry of Fig. 1, the local spatial frequencies are the differences in the direction cosines of the two antenna locations from the phase center divided by the wavelength λ, as indicated in (9). The use of the local spatial frequency is the other half of the technique used by Carter [4] to make 2-D images in the near-field. The work presented here differs only slightly from that in that it just makes the generalization to three dimensions,

$$\mathbf{u}_{J,K} = \frac{1}{\lambda}\left(\frac{\mathbf{R}_J - \mathbf{R}_{PC}}{|\mathbf{R}_J - \mathbf{R}_{PC}|} - \frac{\mathbf{R}_K - \mathbf{R}_{PC}}{|\mathbf{R}_K - \mathbf{R}_{PC}|}\right). \tag{9}$$

The algorithm described above may be ideally suited for security screening of personnel, as in the millimeter waveband the human body is partially reflective and nontransmissive, and clothing is semitransparent. This means the 3-D imaging algorithm would identify the physical location and intensity of a surface in a 3-D volume.

There may be other applications where the bulk of an object is semitransparent and where it may be desirable to generate a volumetric image, such as in a medical application [13]. Here it may be necessary to augment the above 3-D imaging technique with a radiation transport equation inversion if the temperature or emission profile in the human body is to be extracted. A good frequency to do this at might be around 2.5 GHz where the ratio of the skin depth penetration to the half-wavelength spatial resolution in the body is a maximum. However, as the complex refractive index of the human body typically ranges [14] from (2, 0.2) to (7, 0.8) at this frequency, the body is both highly reflective and absorbing. This makes particular challenges for the impedance matching of sensors and the inversion techniques to achieve good sensitivity.

III. Antenna Array Topology

Ideally the visibility function needs to be sampled spatially across the antenna array at the Nyquist spatial frequency to avoid aliasing effects in the imagery. This sampling requirement defines the topology of the antenna array, as samples of the electric field of the radiometric emission are made at the antenna locations. For unidirectional antennas in a single straight line, sampling spatially at every half-wavelength interval corresponds to Nyquist sampling. Under this condition, an alias-free field-of-view exists in a 1-D scene from the perpendicular to the

line, out to a half-angle of $\pi/2$ (i.e., all viewing angles in the plane). If a larger spacing is used, say, d (permitting fewer antennas to be used), this alias-free half-angle, $\theta_{1/2}$ shrinks from $\pi/2$ to that given by $\sin\theta_{1/2} = \lambda/(2d)$. This means that if objects remain within the alias-free field-of-view they will be faithfully reproduced in the image. However, if there are objects outside the alias-free field-of-view, aliases of these will be generated as ghosts within the alias-free field-of-view of the image. In this situation the effects of aliasing can be avoided if there are insufficient levels of emission from objects outside the alias-free field-of-view, or by antenna design, the emission from these regions is not measured. However, for viewing extended targets in the near-field, many low-gain (smaller collection area) antennas will be required to avoid aliasing.

Fully filling an aperture with antennas to satisfy the Nyquist sampling criterion is unnecessary, as all information in a scene up to the diffraction limit (set by the aperture size of the antenna array) is contained in the visibility function, and this can be sampled completely using two types of sparse array. The first type is a minimally redundant array. This uses the smallest number of antennas (for a given aperture size) to measure all spatial frequencies at least once at a single instance in time. This type of array was used to collect experimental data presented here. The other type, a nonredundant array, uses the smallest number of antennas to measure a limited number of spatial frequencies only once, but which through physical movement (of the array or source) collects the remaining spatial frequencies. The nonredundant array is the conventional choice for radio astronomy aperture synthesis. The design of these arrays for aperture synthesis and other sensor systems has been an ongoing area of research for a number of years [15]–[20].

Planar minimally redundant arrays with antennas placed on hexagonal grids were the choice for the experimental systems presented here. The systems were designed initially for making 2-D images in the near-field [21], [22]. The hexagonal grid was the preferred choice for the array, as this enables the closest possible antenna spacing, thus maximizing the size of the alias-free field-of-view. The principal axes of the hexagonal grids of these systems are in directions 0°, 60°, and 120° to the horizontal, as can be seen in Fig. 2. As adjacent rows parallel to the principal axes sample at a half antenna width spacing $(g/2)$, the alias-free half-angle field-of-view $\theta_{1/2}$ is given by (10), where g is the antenna spacing along the axes and λ is the radiation wavelength. Halfway between the principal axes the half-angle alias-free field-of-view $\phi_{1/2}$ is smaller, as the sample interval in these directions increases to $(g/2)\sqrt{3}$, and is given by (11). The complete alias-free field-of-view is approximately hexagonal shaped. The grid spacing in the arrays, from which experimental data are presented here, is 1.2 cm for the 22-GHz system and 7.7 cm for the 94-GHz system. However, simulations have also shown that a small amount of randomization in the position of the antennas on a nominally regular array grid can reduce the impact of aliasing in the image [23],

$$\sin\theta_{\frac{1}{2}} = \frac{\lambda}{g} \tag{10}$$

$$\sin\phi_{\frac{1}{2}} = \frac{\lambda}{g\sqrt{3}}. \tag{11}$$

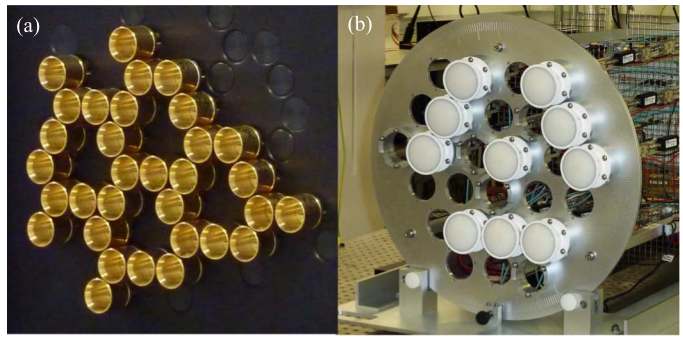

Fig. 2. Antenna arrays of: (a) the 22-GHz 32-channel and (b) 94-GHz 10-channel 3-D aperture synthesis imagers. The heterodyne receivers and cross-correlator are located behind the arrays.

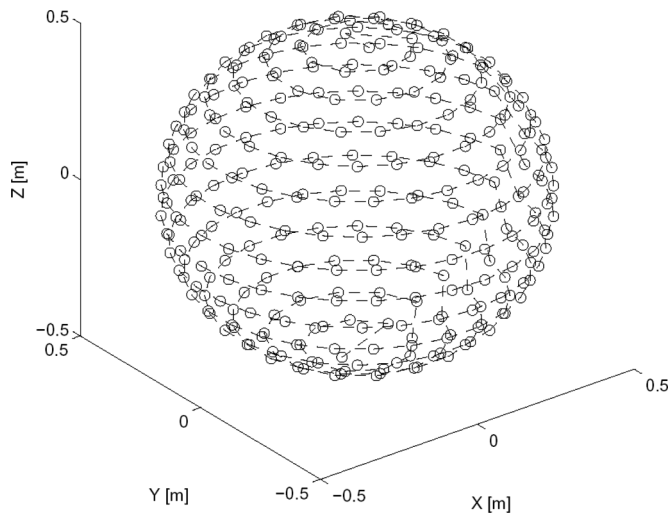

Fig. 3. Spherical array with a diameter of 1 m having 300 equally spaced inward looking antennas sensitive at 22 GHz was used in the simulations of the spatial resolution.

The use of planar antenna arrays for generating 3-D images becomes possible in the near-field, as in this region there are a range of spatial frequencies in the third (z) spatial dimension, as indicated by (9). The demonstration of the 3-D imaging capability arising from this is discussed in Section VI, the experimental validation section of this paper.

The generalization to three dimensions for near-field imaging has the additional benefit that antenna array topology is not restricted to a 2-D (planar) configuration. Antennas can be arbitrarily located in three dimensions (perhaps conformally) to suit individual deployment scenarios, provided sufficient samples are made to minimize the effects of aliasing.

For the purpose of simulating the 3-D imaging capability, a search was not made for a minimally redundant 3-D array. Alternatively, the array chosen for the simulation was an array of 300 inward looking antennas on the surface of a 1-m diameter sphere, as illustrated in Fig. 3. A physically larger minimally redundant version of this, with openings for an entry and exit, might form a suitable antenna array for a walk-through security screening portal [23].

IV. Spatial Resolution

The spatial resolutions possible with this technique are determined from spatial frequencies of the measurement system. A

simplified scenario is considered where the coordinate origin is at the center of an array and the phase center at (X_{PC}, Z_{PC}) is free to move in the z-direction, and is measured by a pair of receivers at locations (X_J, Z_J) and (X_K, Z_K). In this scenario, the spatial frequencies in the x- and z-directions are given directly by (12) and (13) from (9). Here, the $\mathbf{u}$ spatial frequency given in (9) has (x, y, z) components of (u, v, w),

$$u_{J.K} = \left\{ \frac{X_J}{[(Z_{PC}-Z_J)^2+X_J^2]^{\frac{1}{2}}} - \frac{X_K}{[(Z_{PC}-Z_K)^2+X_K^2]^{\frac{1}{2}}} \right\} \frac{1}{\lambda} \tag{12}$$

$$w_{J,K} = \left\{ \frac{Z_{PC}-Z_J}{[(Z_{PC}-Z_J)^2+X_J^2]^{\frac{1}{2}}} - \frac{Z_{PC}-Z_K}{[(Z_{PC}-Z_K)^2+X_K^2]^{\frac{1}{2}}} \right\} \frac{1}{\lambda}. \tag{13}$$

When the source is close to the receivers, the maximum x spatial frequency is achieved when the J, K antenna pair are located along the x-axis on opposite sides of the source. The same is true for the z spatial frequency and the z-axis. In these cases the maximum x and z spatial frequencies from (12) and (13) are both $2/\lambda$ cycles per meter. If all spatial frequencies up to these maxima are measured, the spatial resolutions are the reciprocals of the maximum spatial frequencies, which is $\lambda/2$ in both x- and z- directions, the Abbe microscope resolution. Symmetry arguments indicate this resolution is also achieved in the y-direction. This is equivalent to a numerical aperture of unity in a 2-D lens imaging microscope.

Considering now the source moved out to a large range ($|Z_{PC}| > |Z_J| \sim |Z_K|$), the maximum in the x-component of the spatial frequency from (12) becomes by expansion the reciprocal of the resolution if all spatial frequencies are measured. For a maximum antenna separation of D, this gives (14) for the resolution in the x-direction, which corresponds to the Fraunhofer diffraction limit. By the same argument, expanding (13) for large ranges, the reciprocal of the maximum z-spatial frequency becomes the range resolution of (15). This represents a passive ranging capability, which is enabled by the system sensitivity to wavefront curvature. The uncertainty in range rises as the square of the range, $|Z_{\mathrm{PC}}|$. If it is assumed that a useful ranging capability is lost when the range precision equals the range, (15) indicates that this scenario is reached at a range of one-sixteenth of the Rayleigh Range, where the Rayleigh Range is taken to be $2D^2/\lambda$, the classical discriminator between near- and far-fields. It is therefore concluded that this ranging capability is only useful within the near-field region,

$$\Delta X = \left(\frac{\lambda}{D}\right) |Z_{PC}| \tag{14}$$

$$\Delta Z = 8\lambda \left(\frac{|Z_{PC}|}{D}\right)^2. \tag{15}$$

V. Field-of-View

The field-of-view of this technique in the near-field is limited by the breakdown of the Fresnel approximation. The phase correction applied by (6) followed by the inverse Fourier transform of (5) (equivalent to an inverse Fresnel transform) can no longer be used to create the image. This happens when either the subject size, or the aperture size, or both, become large. Specifically, the phase error $(\Delta\phi)$ in the Fresnel approximation in moving away from the scene center a displacement d, at a perpendicular distance R from the aperture, given by (16), for a wavenumber k $(2\pi/\lambda)$ [24] becomes too large,

$$\Delta\phi = \frac{kd^4}{(2R)^3}. \tag{16}$$

A minimum Fresnel range, R_{FL}, can be defined where the phase error due to the subject (full size) S, and imager aperture diameter D, reaches $\pi/8$ (22.5°), and this is given by (17). This suggests operational limits for the minimum range and the maximum object and array size,

$$R_{FL} = \left[2(D+S)^4/\lambda\right]^{\frac{1}{3}}. \tag{17}$$

However, it further states [24] that a key parameter of near-field diffraction is the Fresnel scale $\sqrt{(\lambda R)}$, and that the majority of the near-field interference pattern is generated from a region approximately four Fresnel scales wide, a more relaxed condition than (17). This indicates that the volume of space that can be imaged using a single inverse Fourier transform may be up to four Fresnel scales in linear dimension. However, multiple adjacent volumes of this size, centered on different phase centers, can be imaged by applying appropriate phase shifts for each volume from (6) to identical sets of cross-correlations before applying the inverse Fourier transform. The Fresnel scale is therefore not a fundamental limitation for the 3-D imaging of arbitrary large objects using this technique. The spatial phase gradients of the correlations from the near-field region, which define the volume of space that can be imaged using a single 3-D Fourier transform, are explored more fully in [25].

VI. Experimental Validation

Experimental data used to validate the 3-D imaging algorithm were generated by aperture synthesis systems operating at the RFs of 22 GHz [21], and 94 GHz [22], developed specifically to explore near-field imaging for security screening of personnel. Both systems, illustrated in Fig. 4, are heterodyne based and use a common IF of 3.71 GHz.

The 22-GHz system, shown in Fig. 4(a), comprises 32 channels and uses a 2-D array of short circular waveguide horn antennas (each having a gain of 9 dBi) on a hexagonal grid having an aperture of approximately 10 cm in diameter, the antenna array being illustrated in Fig. 2(a). A dual stage (sub-harmonic mixing) heterodyne system, having local oscillators (LOs) at 9.4 and 3.71 GHz, mix down a 300-MHz bandwidth from 22 GHz to baseband, where it is sampled by single-bit digitizers in in-phase (I) and quadrature (Q) channels, at a frequency of 330 MHz. Single-bit digitizers were selected, as comprising a single comparator they are relatively inexpensive. They do, however, only deliver 63.7% of the sensitivity possible using ideal Nyquist sampling in comparison to three- and four-level digitization, which deliver 81.0% and 88.1%, respectively [2]. This allows 496 complex cross-correlations to be collected simultaneously in real time. The mean noise temperature of the system over the 32 channels and its standard deviation is 388 $\pm$ 38 K and

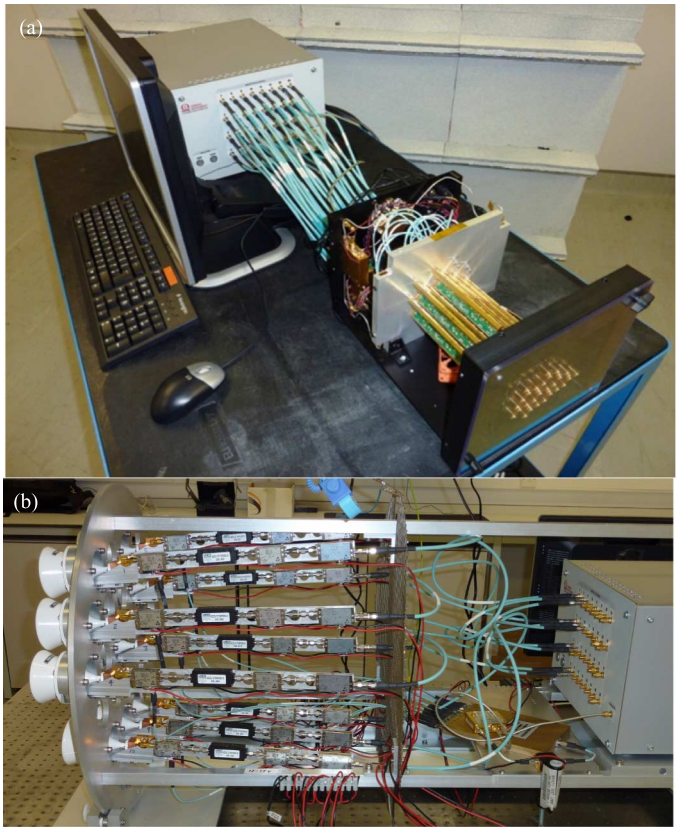

Fig. 4. 22-GHz aperture synthesis imager: (a) comprises 32 channels (black housing at front) connected via IF cables to the single-bit sampling cross-correlator (light colored box at rear). The 94-GHz system: (b) comprises 10 channels using the same sampling and cross-correlator unit. In both systems, the RF, IF, and LO electronics can be seen; the antenna arrays being illustrated in Fig. 2.

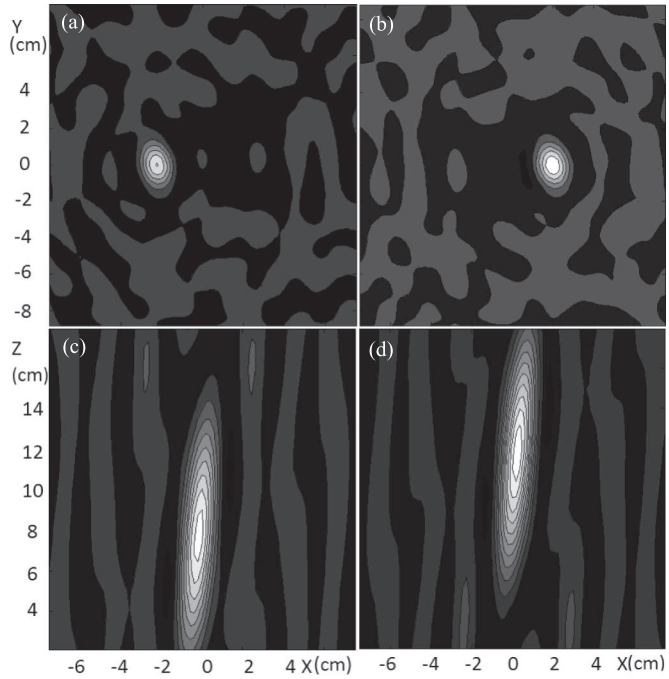

Fig. 5. Image contours at 22 GHz of a noise source in the x–y vertical plane (upper) displaced: (a) -2 cm and (b) $+2$ cm in the x-direction, and in the x–z horizontal plane (lower) displaced: (c) -2 cm and (d) $+2$ cm in the z-direction about a phase center at $x = 0$, $y = 0$, and $z = 10$ cm.

image acquisition time was variable between 5 ms and 10 s. A field programmable gate array (FPGA) is used to cross-correlate electric fields from all $(32 \times 31/2 = 496)$ pairs of receivers and integrate for periods of up to several seconds.

A 25-dB excess noise ratio (ENR) noise source radiating from fundamental waveguide (internal dimensions 4.3 mm by 10.73 mm) at 22 GHz was used as an imaging target, being placed on an axis perpendicular to the center of the array at a distance of 10 cm from the antennas. The source was then moved horizontally from left to right, and closer and further away from the antenna array. Images are generated by putting the phase center a distance 10 cm from the array in the center of the vertical x–y plane. This creates a 3-D set of voxels filling the space before the antenna array. To demonstrate the capability, two planes of images are selected from voxels: 1) the central x–y vertical plane at a range of 10 cm and 2) the x–z horizontal plane along the central axis perpendicular to the antenna array. These images are displayed as grey scaled image contours in Fig. 5 for the source at locations 2 cm to the left and right, and 2 cm forward, and backward of the phase center. The full width at half maximum (FWHM) of the peak in the x–y plane is 1.0 $\pm$0.3 cm and the z-direction it is 9 $\pm$ 1 cm and these are close to the expected resolutions of 1.3 cm $(\sim \lambda)$ and 10 cm from (14) and (15). The slight skewing of the peak in the x–z plane [see Fig. 5(c) and (d)] arises from the asymmetry in the antenna array shown in Fig. 2(a).

The 94-GHz system, shown in Fig. 4(b), comprises 10 channels and uses a 2-D array of circular waveguide horn antennas on a hexagonal grid having a diameter of 39 cm, 32 cm being the longest baseline in the array, the antenna array being illustrated in Fig. 2(b). Each horn antenna has a gain of 35 dBi and uses a lens to focus the beam to a distance of 2 m in front of the array. The system uses two stages of (sub-harmonic) heterodyne mixing with LOs at 45 and 3.71 GHz to sample a 300-MHz bandwidth at 94 GHz. The mean noise temperature of the system over the 10 channels and its standard deviation is 1627 $\pm$ 221 K, a relatively high value for this frequency due to the absence of low-noise RF amplifiers at the front-end. The image acquisition time is variable between 5 ms and 10 s.

A 15-dB ENR noise source radiating from a fundamental waveguide (internal dimensions 1.3 mm by 2.5 mm) was imaged at positions $\pm$3 cm in the x-direction about an (x, y, z) phase center at (0.0, 0.0, 2.0 m) where the origin of the coordinate system is at the center of the array. Images selected for illustration in Fig. 6 are from the 3-D voxel array in the x–y vertical and x–z horizontal planes about this phase center. The images reproduced indicate a movement of the source by $\pm$3 cm in the x-direction. In the x–y plane, the peak has a circular cross section with a FWHM of 2.0 $\pm$ 0.3 cm. This compares favorably with the 2.0-cm resolution given by (14) where D is the longest baseline of 32 cm. The FWHM in the z-direction is 90 $\pm$ 10 cm, which agrees favorably with the value of the resolution given by (15) of 100 cm.

For the 22-GHz aperture synthesis imager, an x-dimension field-of-view of $\pm$2 cm was demonstrated (Fig. 5) at a range of 10 cm from the array, while the Fresnel scale for this range is 3.64 cm. For the 94-GHz imager, the x-direction field-of-view

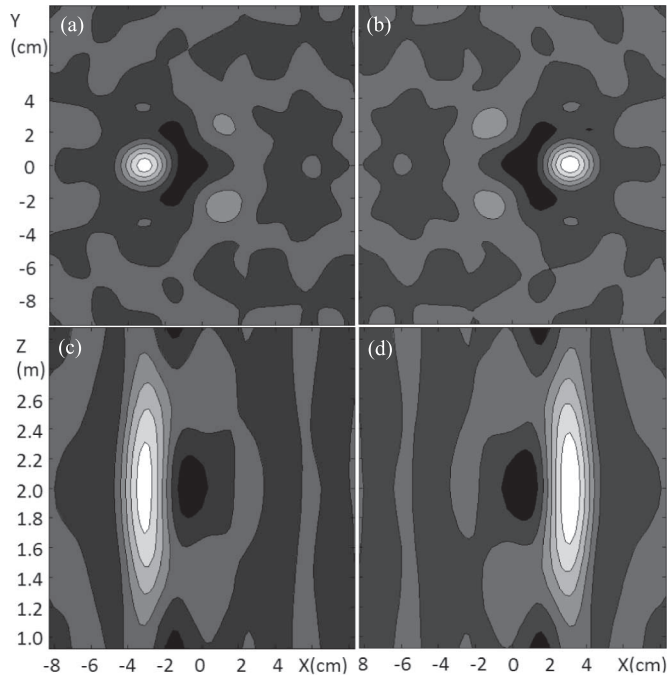

Fig. 6. Image contours at 94 GHz of a noise source in the x–y vertical plane (*upper*) and x–z horizontal plane (*lower*) displaced: (a) and (c) -3 cm and (b) and (d) $+2$ cm in the x-direction about a phase center at the $x = 0$, $y = 0$, and $z = 2$ m.

of ± 3 cm was demonstrated (Fig. 6) at a range of 2.0 m, while the Fresnel scale for this measurement was 8 cm. In both experiments, moving the noise source to greater off-axis distances to explore wider fields-of-view resulted in image degradation due to the predictable effects of aliasing. For this reason it was not possible to distinguish the effects of Fresnel approximation breakdown from that of aliasing. Therefore it can only be stated here that the image field-of-view perpendicular to range in these experiments is of the order of the Fresnel scale.

Although this experimental validation has been conducted with a noise source it is considered representative of a point thermal source as it is temporally incoherent. A point source, which by definition is spatially coherent, is considered suitable for demonstrating the resolution of systems designed to image extended sources. This is because the VCZ theorem, upon which the technique is based, only requires an extended source to comprise a multitude of spatially coherent sources, which have random phase relations. The demonstration of aperture synthesis systems to generate 2-D images of point and extended sources in the near- and far-field is presented in [21] and [22]. Comparisons of measured radiometric temperature sensitivities agree well with the standard aperture synthesis radiometer equation [21]. A key next milestone for this research is to demonstrate 3-D imaging of extended 3-D sources.

VII. Simulations of 3-D Imaging

Simulation of radiometric aperture synthesis imaging is possible because the emission from a scene is generated by a multitude of sources having random phase relations. When this emission arrives at the antenna locations and the cross-correlations of (1) are formed, a large number of terms are generated for each cross-correlation. However, because the phase relations of the sources are random and tens of millions of cross-correlations are integrated for each image frame, the cross-terms vanish. The remaining term for each cross-correlation is a summation over all sources S in the field-of-view of the product of the amplitude (voltage) reception pattern for each pair of antennas $g_{J,S}g_{KS}$, the intensity of the source I_S, and the exponent of the phase difference corresponding to the distances between the source and the two antennas $\phi_{J,S} - \phi_{K,S}$ divided by product of the distances to the source from the two antennas $r_{J,S}r_{K,S}$ [26], as described by (18). The sizes of the sources in the field of view can be made just slightly smaller than the spatial resolution of the system so the simulation is not sensitive to the discretization of the objects. This means the generation of simulated cross-correlations from hundreds of antennas from a synthetic scene with hundreds of thousands of pixels (or voxels) is possible in a standard personal computer. These synthetic cross-correlations can then be processed into 3-D images using the algorithm in Section II,

$$V'_{J,K} = \sum_{All\ S} \frac{g_{J,S}g_{K,S}I_S}{r_{J,S}r_{K,S}} \exp\left[i(\phi_{J,S} - \phi_{K,S})\right]. \qquad (18)$$

Simulations are performed to investigate the limits of the spatial resolution and the field-of-view of the 3-D imaging technique. For this purpose, a spherically symmetrical array of 300 antennas with a primary gain of 9 dBi, depicted in Fig. 3, was used. A frequency of 22 GHz was chosen, as its wavelength is close to the desired spatial resolution for security screening and the cost of receivers is relatively low [27]. The phase center, which forms the center of the 3-D image, was placed at the center of this array.

To investigate the resolution, the point-spread function of the system was estimated by imaging a point source at the center of the array. Synthetic cross-correlations from this were generated and processed into an image using the algorithm of Section II. This image, representing the point-spread function, has some negative values, as is possible in aperture synthesis systems [28]. The spatial extent of the point-spread function in an x–y slice (of the 3-D image) at $z = 0$ is shown on a log scale of the absolute values in Fig. 7(a). The first dark ring from the image center represents the first zero crossing of the point spread function and the first bright ring (the first minimum) represents the Rayleigh resolution [29], which by analysis is found to be at a radius of $\lambda/2.09 \pm 10\%$ from the center.

Sensitivity to the change in point-source position was investigated by examining the phase of the visibility function. Keeping the phase center at the center of the array, the point source was moved a distance of 1 mm in the y-direction. A slice in the $u_1 - u_2$ spatial frequency plane (corresponding to the x–y plane) at $u_3 = 0$ of the 3-D visibility function for this simulation is shown in Fig. 7(b). The values of the measured visibility function lie on a plane surface tilted in the u_2 direction. The gradient of the tilt seen from this plot is 1 mm, the displacement of the point source in the plane. It can be seen in this plot that in the corner regions of the FFT grid the phase of the visibility function has been set to zero, as no data are present in these locations, as discussed in Section II.

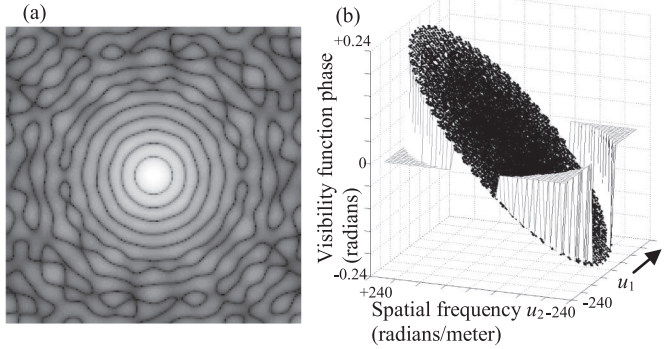

Fig. 7. Simulation showing: (a) x–y slice at $z = 0$ through the 3-D image (on a log scale of absolute values) of a point source at the center of the array in Fig. 3 and (b) surface plot of a $u_1 - u_2$ slice at $u_3 = 0$ through the visibility phase function $V(\mathbf{u})$ when the point source is displaced 1 mm in the y-direction from the array center.

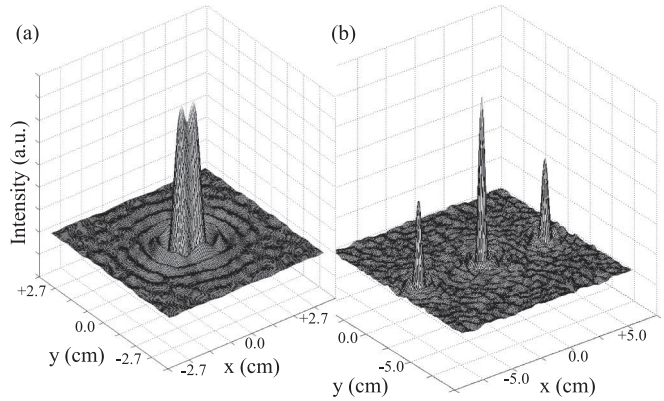

Fig. 8. Simulations of the 3-D intensity $I(\mathbf{l})$ showing the x–y slices at $z = 0$ as surface plots for: (a) two closely spaced point sources demonstrating the sparrow resolution limit and (b) three point sources illustrating the Fresnel limit on the field-of-view.

The spatial resolution of the system was further examined by simulating the Sparrow resolution limit [29]. Two closely spaced point sources centered on the array center were simulated and their spacing reduced until the two discrete sources were barely discernable. The resulting image for this scenario is illustrated in Fig. 8(a) and the spacing of the sources, which defines the Sparrow resolution, is measured at 6.01 ± 0.60 mm or $\lambda/2.21 \pm 10\%$. This is just slightly smaller than the measured Rayleigh resolution. Simulations at frequencies from 3 to 300 GHz and for arrays of dimensions ranging from 0.3 to 3 m in diameter showed the same $\sim \lambda/2$ resolution limit. These values support the statement that the spatial resolution at the center of the array is that of the half-wavelength Abbe resolution limit for a numerical aperture of unity [29].

Using the same simulation program, it was shown that the spatial resolution of the 22-GHz array of Fig. 2 at a 10-cm range is close to that predicted by (14) and (15). Reducing the antenna gain in the simulation to 0 dBi indicates the resolution directly adjacent and parallel to the array approaches the $\lambda/2$ limit.

The field-of-view limitation, as predicted by the breakdown of the Fresnel approximation, was simulated by placing three point sources in a line through the array center. The spherical array had 300 antennas, but for this particular simulation the array radius was 30 cm. The two outer sources were moved apart symmetrically, while the central one remained at the array center. As the spacing between the sources increased, the image intensity of the two outer sources fell. This reduction is not due to the antenna pattern, but due to the breakdown in the Fresnel approximation. It should also be noted that the widths of peaks from the two outer point sources is the same as that of the central peak so resolution does not change in moving that distance away from the array and phase center. The simulated image as a surface plot when the intensity of the two outer sources had reduced to 50% of the central source is illustrated in Fig. 8(b). The full width between the two outer sources for this scenario is 11 cm. The Fresnel scale $\sqrt{(\lambda R)}$ for this scenario, where R is taken to be the array radius, is 6.32 cm so the full field-of-view width is approximately two Fresnel scales.

Simulations of 2-D extended sources in the near-field are described in [23], [26], and [27]. Current research is simulating 3-D imagery from extended 3-D sources in the near-field, to understand and mitigate noise in the images, so levels approach those predicted by the radiometer (3) for sparse arrays. Algorithms are being investigated to identify radiating surfaces in the 3-D images with a view to offering full body images of security screening subjects from any perspective direction (including from below), making under-clothing concealment of threats on any part of the body difficult. A further security application currently under investigation exploits the transparency of canvas and fiber glass for the screening of vehicles for stowaways.

On the technology front, digital signal-processing architectures using FPGAs are being investigated that can generate cross-correlations from hundreds of receiver channels on nanosecond timescales. Funding is sought to develop systems with antenna array geometries that can demonstrate the half-wavelength spatial resolution in 3-D, image extended targets in the near-field, and develop systems for commercial security screening.

VIII. Conclusions

A technique to image in three dimensions using aperture synthesis has been presented and validated using simulations and experimental demonstrations at 22 and 94 GHz. The technique enables the Abbey microscope resolution $(\lambda/2)$ in three dimensions to be achieved and a passive ranging capability. This will enable new architectures of passive sensors to screen persons for concealed threats, in portal and stand-off scenarios, operating in the millimeter waveband, where clothing is semi-transparent. The technique could also be developed for other spectral regions, for example, in the microwave band for medical imaging. The emerging FPGA and application specific integrated circuit (ASIC) digital processors are a means to realizing the cross-correlators in a compact format for these new aperture synthesis architectures.

References

[1] M. Born and E. Wolf, "Partially coherent light," in *Principles of Optics*, 7th ed. Cambridge, U.K.: Cambridge Univ. Press, 2003.

[2] A. Thomson, M. Moran, and G. Swenson, "Analysis of the interferometer response," in *Interferometry and Synthesis in Radio Astronomy*. New York, NY, USA: Wiley, 2004.

[3] W. H. Carter and E. Wolf, "Correlation theory of wavefields generated by fluctuating, three-dimensional, primary, scalar sources," *Opt. Acta*, vol. 28, no. 2, pp. 227–224, 1981.
[4] W. H. Carter, "On refocusing a radio telescope to image sources in the near field of the antenna array," *IEEE Trans. Antennas Propag.*, vol. 37, no. 3, pp. 314–319, Mar. 1989.
[5] A. M. Zarubin, "Three-dimensional generalization of the van Cittert-Zernike theorem to wave and particle scattering," *Opt. Commun.*, vol. 100, no. 5–6, pp. 491–507, 1993.
[6] J. Rosen and A. Yariv, "Three-dimensional imaging of random radiation sources," *Opt. Lett.*, vol. 21, no. 14, pp. 1011–1013, 1996.
[7] D. L. Marks, R. A. Stack, and D. J. Brady, "Three-dimensional coherence imaging in the Fresnel domain," *Appl. Opt.*, vol. 38, no. 8, pp. 1332–1342, 1999.
[8] T. S. Ralston, D. L. Marks, P. S. Carney, and S. A. Boppart, "Interferometric synthetic aperture microscopy," *Nature Phys.*, vol. 3, pp. 129–133, Feb. 2007.
[9] F. Natterer and F. Wübbeling, "Tomography," in *Mathematical Methods in Image Reconstruction*. Philadelphia, PA, USA: SIAM, 2001.
[10] C. S. Ruf, C. T. Swift, A. B. Tanner, and D. M. Le Vine, "Interferometric synthetic aperture microwave radiometry for the remote sensing of the earth," *IEEE Trans. Geosci. Remote Sens.*, vol. 26, no. 5, pp. 597–611, Sep. 1988.
[11] D. M. Le Vine, M. Kao, A. B. Tanner, C. T. Swift, and A. Griffis, "Initial results in the development of a synthetic aperture microwave radiometer," *IEEE Trans. Geosci. Remote Sens.*, vol. 28, no. 4, pp. 614–619, Jul. 1990.
[12] J. W. Goodman, "Analysis of two-dimensional signals and systems," in *Introduction to Fourier Optics*, 3rd ed. Greenwood Village, CO, USA: Roberts & Company, 2005, pp. 15–18, Ch. 2.
[13] N. C. Haslam, A. R. Gillespie, and C. G. T. Haslam, "Aperture synthesis thermography—A new approach to passive microwave temperature measurements in the body," *IEEE Trans. Microw. Theory Techn.*, vol. MTT-32, no. 8, pp. 829–834, Aug. 1984.
[14] C. Gabriel, S. Gabriel, and E. Corthout, "The dielectric properties of biological tissues: I. Literature survey," *Phys. Med. Biol.*, vol. 41, no. 11, pp. 2231–2249, 1996.
[15] M. J. E. Golay, "Point arrays having compact, nonredundant autocorrelations," *J. Opt. Soc. Amer.*, vol. 61, pp. 272–273, 1971.
[16] T. J. Cornwell, "A novel principle for optimization of the instantaneous fourier plane coverage of correlation arrays," *IEEE Trans. Antennas Propag.*, vol. 36, no. 8, pp. 1165–1167, Aug. 1988.
[17] C. S. Ruf, "Numerical annealing of low-redundancy linear arrays," *IEEE Trans. Antennas Propag.*, vol. 41, no. 1, pp. 85–90, Jan. 1993.
[18] Y. Meurisse and J.-P. Delmas, "Bounds for sparse planar and volume arrays," *IEEE Trans. Infor. Theory*, vol. 47, no. 1, pp. 464–468, Jan. 2001.
[19] L. E. Kopilovich and L. G. Sodin, "Interferometers with complete coverage of symmetrized domains in the U,V -plane," in *Multielement System Design in Astronomy and Radio Science*. New York, NY, USA: Springer, 2001.
[20] A. B. Meinel and M. P. Meinel, "Optical phased array configuration for an extremely large telescope," *Appl. Opt.*, vol. 43, no. 3, pp. 601–607, 2004.
[21] N. A. Salmon *et al.*, "First video rate imagery from a 32-channel 22-GHz aperture synthesis passive millimetre wave imager," in *Proc. SPIE Eur. Security + Defence, Millim. Wave, Terahertz Sens. Technol. IV*, Prague, Czech Republic, 2011, vol. 8188, no. 05, pp. 1–12.
[22] N. A. Salmon *et al.*, "First imagery generated by near-field, real-time aperture synthesis passive millimetre wave imagers at 94 GHz and 183 GHz," in *Proc. SPIE Eur. Security + Defence, Millim. Wave, Terahertz Sens. Technol. III*, Toulouse, France, 2010, vol. 7837, no. 01, pp. 1–12.
[23] N. A. Salmon and N. Bowring, "Near-field and three-dimensional aperture synthesis imaging," in *Proc. SPIE Eur. Security +Defence, Millim. Wave, Terahertz Sens. Technol. VI*, Dresden, Germany, 2013, vol. 8900, pp. 1–9.
[24] A. Papoulis, "Fresnel Diffraction," in *Systems and Transforms With Applications in Optics*. New York, NY, USA: McGraw-Hill, 1968.
[25] N. A. Salmon, "Near-field aperture synthesis millimeter wave imaging for security screening of personnel," in *9th Int. Commun. Syst., Netw., Digital Signal Process. Symp.*, Jul. 23–25, 2014, pp. 1082–1085.
[26] N. A. Salmon, P. N. Wilkinson, and C. Taylor, "Interferometric aperture synthesis for next generation passive millimetre wave imagers," *Proc. SPIE*, vol. 8544, no. 05, pp. 1–10, 2012.
[27] N. A. Salmon and N. Bowring, "Three-dimensional radiometric aperture synthesis microscopy for security screening," in *Proc. SPIE Eur. Security + Defence, Millim. Wave, Terahertz Sens. Technol. VII*, Amsterdam, Holland, 2014, vol. 9252, no. 04, pp. 1–9.
[28] A. Labeyrie, S. G. Lipson, and P. Nisenson, "Aperture synthesis," in *An Introduction to Optical Stellar Interferometry*, 1st ed. Cambridge, U.K.: Cambridge Univ. Press, 2006.
[29] A. Lipson, S. G. Lipson, and H. Lipson, "Image formation," in *Opt. Phys.*, 4th ed. Cambridge, U.K.: Cambridge Univ. Press, 2011.

Neil A. Salmon, photograph and biography not available at the time of publication.